Wideband Metasurface-based Fabry-Perot Resonant Cavity Antenna with Polarization Reconfigurable Controlled by Diodes and Resistors

Zhendong Ding, Jiawang Li, Hao Wang, *Member, IEEE*, Nasimuddin Nasimuddin, *Senior Member, IEEE*, Wenjie Feng, *Senior Member, IEEE*, Wenquan Che, *Fellow, IEEE*, and Quan Xue, *Fellow, IEEE*

***Abstract*—A broadband high gain metasurface-based Fabry-Perot resonant cavity antenna (FPRCA) for polarization reconfigurable is proposed in this paper. The antenna features a microstrip source antenna with a single-layer 2×2 circular patch metasurface, a ground plane, a double-layer partially reflective surface (PRS), along with four resistors and two diodes. Characteristic mode analysis (CMA) is performed on a 2×2 circular patch metasurface, and the design is optimized to ensure that the characteristic currents of its modes are orthogonal, enabling effective excitation of circular polarization (CP). In addition, further research through CMA has found that adding loads can change the direction of current orthogonal to each other, thereby achieving the polarization reconfigurable characteristics of the antenna. The designed double-layer PRS generates a positive reflection phase gradient and can radiate CP waves. The proposed unloaded device antenna achieves a -10 dB impedance bandwidth (IBW) of 20.6%, a 3-dB axial ratio bandwidth (ARBW) of 17.2%, a peak gain (PG) of 12.0 dBic at 7.7 GHz, and a 3-dB gain bandwidth of 19.7%. By connecting 100Ω resistors, linear polarization (LP) is achieved, with a -10 dB IBW of 14.6% and a PG of 6.0 dBi at 7.7 GHz. When the access PIN diodes are activated, the antenna achieves left-handed circular polarization (LHCP), exhibiting -10 dB IBW of 21.0%, a 3-dB ARBW of 18.4%, and a PG of 11.8 dBic at 6.9 GHz.**

***Index Terms*—Characteristic mode analysis, Fabry-Perot, metasurface, partially reflective surface, reconfigurable.**

I. Introduction

TRADITIONAL antennas [1], [2] face significant challenges in achieving high-performance requirements. Although patch antennas [3], [4] offer advantages such as simple structure and easy integration, they face significant limitations in gain enhancement. This makes them inadequate for applications requiring long-distance communication or high-precision detection. To address these performance bottlenecks, researchers have continued to explore innovative antenna structures and technologies, leading to the development of Fabry-Perot resonant cavity antennas (FPRCAs) [5]-[7]. In wireless communication systems, antennas are required to exhibit high gain, wide bandwidth, and strong directionality to support high-speed [8], high-capacity data transmission [9] and wide-angle coverage [10]. The FPRCA leverages the resonant characteristics of the resonant cavity to enhance radiation efficiency [11], increase gain [12], widen bandwidth [13], and reduce signal fading and interference [14], thereby meeting the stringent performance requirements of next-generation communication systems.

Fig. 1. Applications scenarios for of antenna polarization.

Over the past decades, the development of FPRCAs has advanced toward multifunctional and high-performance designs. Current research efforts focus on several key technological directions, including the expansion of the 3-dB gain bandwidth [15], [16], low profile design and cavity height reduction [17], [18], shared aperture [19], [20], CP [21], [22], beam control [23], [24], and reconfigurable [25]. Among these,

Manuscript received October 29, 2025. This work was supported in part by the Postgraduate Research & Practice Innovation Program of Jiangsu Province in China (KYCX23_0467). (Corresponding author: *Wenjie Feng*)

Zhendong Ding, Wenjie Feng, Wenquan Che and Quan Xue are with Guangdong Provincial Key Laboratory of MillimeterWave and Terahertz, School of Electronic and Information Engineering, South China University of Technology, Guangzhou 510640, China (e-mail: eezdding@scut.edu.cn; fengwenjie1985@163.com).

Hao Wang is with the School of Electronic and Optical Engineering, Nanjing University of Science and Technology, Nanjing 210094, China (e-mail: haowang@njust.edu.cn).

Jiawang Li is with the Department of Electrical and Information Technology, Lund University, Lund 22100, Sweden (e-mail: jiawang.li@eit.lth.se).

Nasimuddin is with the Institute for Infocomm Research, A*STAR, Singapore 138632 (e-mail: nasimuddin@a-star.edu.sg).

the integration of metasurface into Fabry-Perot has proven particularly impactful, offering significant advantages across multiple dimensions. Metasurface contributes notably to low profile antenna designs by enabling thinner cavity structures, which reduces spatial requirements and facilitates integration in compact systems. In beam control applications, metasurface can precisely manipulate the direction and shape of the radiated beam, thereby enhancing the radiation performance and adaptability of the antenna. Furthermore, they are instrumental in broadening the operational bandwidth and achieving higher gain levels. Beyond these enhancements, metasurface also supports the realization of dual-frequency or multi-frequency operation, addressing the growing demand for multi-band functionality in modern communication systems. Collectively, these capabilities underscore the critical role of metasurface in advancing the performance and versatility of FPRCAs.

In wireless communication systems, the polarization state plays a critical role, as illustrated in Fig. 1. Polarization techniques are foundational to modern communication technologies and influence performance across all layers of wireless systems. To enable polarization state switching and achieve multifunctional capabilities, reconfigurable antennas have become indispensable. These antennas are categorized into four main types: frequency reconfigurable [26], [27], pattern reconfigurable [25], [28]-[31], polarization reconfigurable [25], [32]-[34], and performance hybrid reconfigurable [35]-[37]. Various technologies have been employed to realize antenna reconfigurability. Among them, PIN diodes have the most widely used in [25], [27]-[29], [35]-[37], in addition to capacitors [26], resistors [38], dielectric resonators [33], and mechanical rotating structures [34]. For polarization reconfigurable designs, a range of configurations has been demonstrated. For example, six PIN diodes and three inductors were used to switch between LP and CP in [32]. In [36], 16 PIN diodes enabled switching between vertical polarization (VP) and horizontal polarization (HP). A more complex system with 684 PIN diodes achieved polarization control in x-, y-, and 45° directions in [25]. Additionally, liquid metal flow mechanisms have been used to switch between left-handed circular polarization (LHCP), right-handed circular polarization (RHCP), and LP in [39].

TABLE I
QUANTITATIVE ANALYSIS OF CMA FOR RELEVANT RECONFIGURABLE ANTENNAS

Indicator	2023/[40]	2024/[41]	2024/[42]
Core Function	Frequency reconfigurable	Dual port decoupling and frequency-reconfigurable	Wideband polarization reconfigurable
CF (GHz)	2.55	5.14	2.7
DM MS (CF)	0.85 (CM2)	0.82 (CM1+CM2)	0.62 (CM1+CM2)
ERBW (GHz)	0.13~0.16	0.17	1.48
DM RRAL (%)	78	88.5	85.3
MRA (%)	75	82	75
MO	3rd order Mode 1-3	2nd order Mode 1-2	4th order Mode 1-4

CF: Center Frequency. DM: Dominant Mode. ERBW: Effective Resonance Bandwidth. RRAL: Retention Rate After Loading. MRA: Modal Regulation Accuracy. MO: Modal Order.

From an analytical perspective, CMA has recently emerged as a valuable tool in antenna design. CMA has been applied to various types of reconfigurable antennas [40]-[42]. However, in most reported works, only a single polarization state is analyzed, and comprehensive post-integration analyses-especially after device loading-are generally lacking, as noted in [42]. The relevant quantitative comparisons are shown in Table I. This indicates that the application of CMA for reconfigurable-antenna analysis remains incomplete and requires further exploration. In addition, the integration of high-performance FPRC structures with metasurface offers a frontier avenue for advancing reconfigurable antenna design, providing the potential for enhanced gain, bandwidth, and polarization agility.

A broadband high gain polarization reconfigurable FPRCA is proposed, which is based on the reference [43] by adding PIN diodes to achieve another polarization switching, and additionally adding in-depth analysis of characteristic modes. Based on CMA, research has found that single-layer 2×2 circular metasurface plays a key role in exciting CP characteristics in antenna systems. At the same time, the designed double-layer PRS is a positive reflection phase gradient, which can effectively radiate CP waves. Due to the crucial role of circular unit cell-based metasurface in generating CP, four resistors and two diodes were cleverly connected between the circular metasurface units. Through in-depth analysis using CMA, it is observed that the integration of resistors and diodes alters the orthogonal current distributions within the circular metasurface. This enables the successful realization of polarization reconfigurability in the antenna. The proposed design effectively combines broadband operation, high gain, and polarization reconfigurability, owing to its innovative structure and strategic component placement. The proposed design effectively combines broadband operation, high gain, and polarization reconfigurability, due to its innovative structure and strategic component placement.

II. Design and Analysis of the Proposed Antenna

A. Geometry and mechanism of the proposed antenna

Fig. 2 illustrates the decomposition structure of the proposed antenna. It consists of four layers F4B substrate (relative dielectric constant ε_r=2.65, loss tangent $tan\delta$=0.0015), with a planar size of 60 mm×60 mm, which is fed by a 50Ω SMA joint microstrip line. The first substrate is a microstrip antenna, while the second substrate consists of a 2×2 circular metasurface designed to excite CP, together forming the source antenna. The third and fourth substrates are PRS, which enhance the gain and facilitate radiation of CP waves. Four resistors are symmetrically distributed to enable reconfigurability, allowing antenna to switch between LP and CP, while maintaining consistent impedance bandwidth and polarization states across the dual ports. Secondly, after loading two PIN diodes, the antenna achieves LHCP characteristics. CMA is employed to analyze the underlying principles of both CP and LP.

Fig. 3 depicts radiation mechanism schematic of the proposed FPRCA with PRS. When the FP resonant cavity satisfies the resonance condition Equation (1) in [44], it fully transmits the incident wave at a specific frequency. However, when the frequency of the incident wave deviates from the resonant frequency, the resonant cavity exhibits varying degrees of reflection.

$$-\frac{4\pi h_{cav}}{\lambda}+\varphi_1+\varphi_2=2N\pi, N=0,1,2\cdots \tag{1}$$

where, h_{cav} is the height of the resonant cavity, corresponding to the wavelength of the resonant frequency in vacuum, φ_1 and φ_2 are the reflection phases of the reflective layer and floor, respectively, and N is the resonant mode. According to [45], the resonant frequency of a single point is calculated as

$$f_0=\frac{c}{4\pi h_{cav}}(\varphi_1+\varphi_2-2N\pi) \tag{2}$$

where, c is the speed of light in free space. According to theoretical formulas, the height of the resonant cavity is approximately half the wavelength of the resonant frequency.

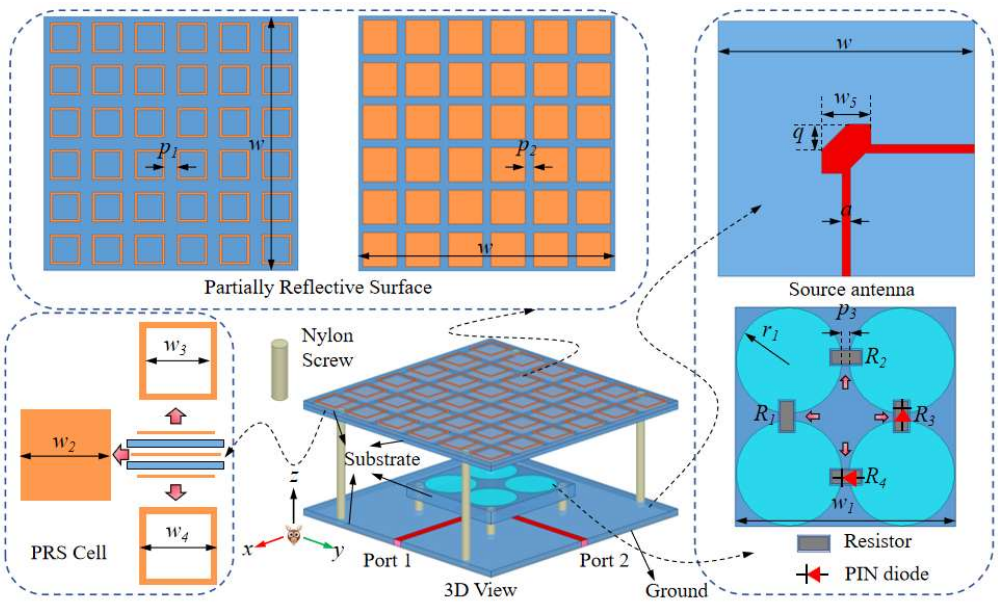

Fig. 2. The topology of the proposed broadband polarization reconfigurable FPRCA. The dimensions are w = 60, h_1 = 1.5, h_2 = 3, h_3 = 1, h_4 = 1, H_{cav} = 21, H_{air} = 3, w_1 = 25, w_2 = 8, w_3 = 7, w_4 = 6, w_5 = 11.5, p_1 = 3, p_2 = 2, p_3 = 0.8, q = 6, a = 2, r = 6, (unit: mm).

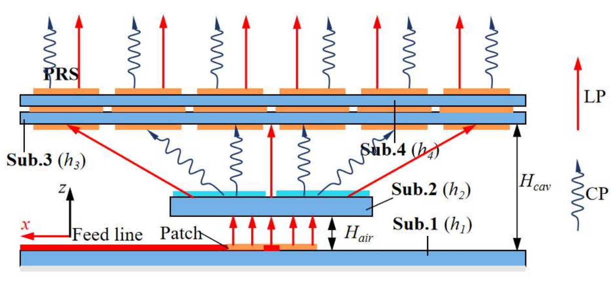

Fig. 3. Radiation mechanism schematic of the proposed antenna.

B. The design and analysis of the source antenna

Fig. 4 shows the evolutionary process of source antenna design. For ordinary microstrip antennas, the length W and width L of the patch are crucial for antenna resonance. For antenna I, due to its equal length and width, the resonant frequency can be calculated as follows:

$$\varepsilon_e=(\varepsilon_r+1)+(\varepsilon_r-1)(1+10h/a)^{-\frac{1}{2}} \tag{3}$$

$$\Delta l=0.412h\left(\frac{\varepsilon_e+0.3}{\varepsilon_e-0.258}\right)\left(\frac{w/h+0.264}{w/h+0.8}\right) \tag{4}$$

$$f_c=c/(2(w+2\Delta l)\sqrt{\varepsilon_e}) \tag{5}$$

where, ε_r is the relative dielectric constant of the substrate, ε_e is the effective dielectric constant, and h is the height of the dielectric substrate.

Antenna I is a conventional patch antenna and based on the calculated dimensions and resonant frequency, its resonance is around 7.5 GHz. However, as shown in Figs. 4 (a)-(b), the resonance performance is suboptimal and does not meet the desired specifications. To improve the axial ratio, the antenna is modified by chamfering corners (antenna II), as shown in Fig.

4(c). The axial ratio was relatively improved but still did not achieve the desired effect. The reason is that the feeding transmission line is too long, resulting in excessive transmission loss and poor reflection. Even if the angle is cut, CP waves cannot be successfully excited. Therefore, further improvements will be made to antenna II by introducing a 90° transmission line to obtain antenna III. The simulation results are shown in Figs. 4(a)-(b), with a -10 dB IBW of 6.64 GHz~8.29 GHz (22.1%), in band gain of 3.3~5.6 dBi, and an axial ratio close to 3 dB. The CP wave has not been exciting and further improvement is needed. Considering that the desired effect was not achieved after adjusting the single-layer structure, a metasurface is introduced.

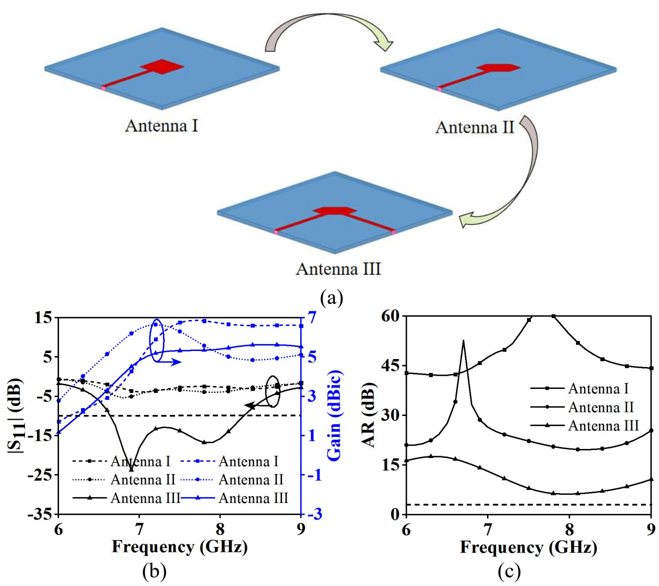

Fig. 4. The evolution process of the source antenna design: (a) three types of single-layer antennas, (b) $|S_{11}|$ and gain, and (c) AR.

CMA is a recently emerged method for auxiliary antenna design and analysis [46]. It combines the advantages of numerical and analytical methods for solving complex electromagnetic problems. The inherent characteristics of conductor structures can be determined without external excitation, serving as a valuable tool in metasurface analysis. In broadband and CP studies, mode significance (MS) helps identify potential resonant modes. Moreover, the orthogonality of characteristic currents offers the potential to generate CP waves. MS is defined as

$$\text{MS} = \left|1/(1+j\lambda_n)\right| \tag{6}$$

For the mode resonance state, the MS is equal to 1; when MS≥0.707, the corresponding frequency range is considered the resonant bandwidth, indicating strong potential for resonance and ease of excitation. In contrast, when MS<0.707, the frequency range is classified as non-resonant, characterized by weak resonance behavior, low potential for excitation, and reduced susceptibility to external stimulation. The f_H is the high-end frequency of the resonance, the f_L is the low-end frequency of the resonance, and the following conditions are met

$$\text{MS}(f_H) = \text{MS}(f_L) = 1/\sqrt{2} \tag{7}$$

Due to the limited ability of single layer microstrip antennas to excite CP waves, a symmetric metasurface structure is used to enhance CP wave excitation. CMA is employed for both analysis and design. Since the resonant bandwidth of the antenna has already been determined, the MS must exhibit a comparable resonant bandwidth to ensure effective performance. As illustrated in Fig. 5, the first six modes were analyzed. Modes 1 and 2 overlap and exhibit characteristics consistent with the CMA behavior of symmetric metasurface. Their resonance occurs at 7.06 GHz, with a bandwidth ranging from 6.32 GHz to 8.46 GHz-closely matching the resonant bandwidth of Antenna III. Modes 3 through 6 acts as auxiliary higher-order modes. Modes 1 and 2 form a pair of orthogonal modes, and their orthogonality in surface current distribution can be expressed as follows

$$\langle \mathbf{J}_1, \mathbf{R}\cdot\mathbf{J}_2 \rangle = \langle \mathbf{J}_1^*, \mathbf{R}\cdot\mathbf{J}_2 \rangle = 0 \tag{8}$$

$$\langle \mathbf{J}_1, \mathbf{X}\cdot\mathbf{J}_2 \rangle = \langle \mathbf{J}_1^*, \mathbf{X}\cdot\mathbf{J}_2 \rangle = 0 \tag{9}$$

$$\langle \mathbf{J}_1, \mathbf{Z}\cdot\mathbf{J}_2 \rangle = \langle \mathbf{J}_1^*, \mathbf{Z}\cdot\mathbf{J}_2 \rangle = 0 \tag{10}$$

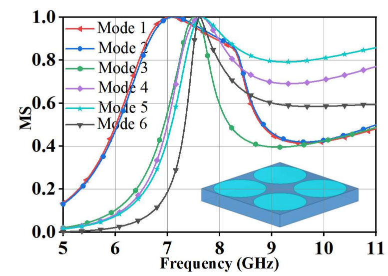

Fig. 5. Six modes MSs of 2×2 circular patch metasurface.

To excite CP, it is essential to observe the characteristic current directions of a pair of orthogonal models. As shown in Fig. 6, the characteristic currents at 7.5 GHz reveal that Modes 1 and 2 are oriented at a 90° angle to each other, indicating their capability to generate CP waves. Modes 3, 4, 5, and 6 also exhibit mutually orthogonal current distributions, with some components canceling each other out; therefore, they serve an auxiliary role in CP generation. The metasurface and microstrip antenna are separated by an air gap to form a cavity that facilitates CP excitation, as illustrated in Fig. 7(a). Figs. 7(b)-(c) show an IBW of 6.72 GHz ~8.35 GHz (21.6%), the gain of 5.3 GHz ~8.1 dBic in band, the radiation efficiency greater than 90%, and ARBW of 7.25 GHz ~8.34 GHz (14.0%).

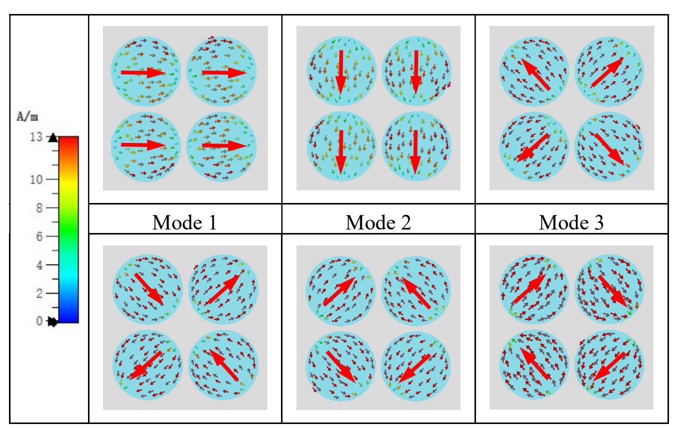

	Mode 4	Mode 5	Mode 6

Fig. 6. Six modes current distributions of the 2×2 circular patch metasurface at 7.5 GHz.

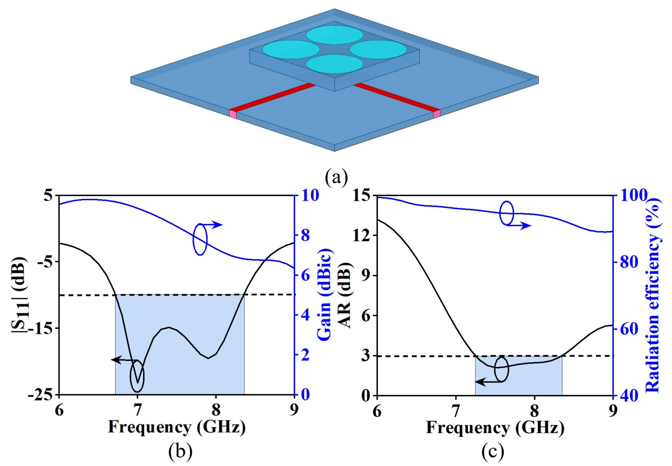

Fig. 7. The design of the source antenna: (a) the antenna model, (b) $|S_{11}|$ and gain, and (c) AR and radiation efficiency.

C. The design and analysis of the partially reflective surface

The detailed configuration of the PRS unit structure is shown in Fig. 8. The substrate is made of F4B material, with a thickness of h_3=h_4=1 mm and a relative dielectric constant of 2.65. FSS units are etched onto the dielectric substrate, which features a two-layer stacked design. Identical square groove patches are placed on both the top and bottom surfaces, with an additional square patch embedded at the middle layer.

The equivalent analysis of the unit structure is illustrated in Fig. 9. When electromagnetic waves are incident perpendicularly onto the PRS of the antenna, the FSS printed on the top, middle, and bottom layers of the substrate can be modeled as a parallel multilayer structure. Let η_0 to represent the wave impedance of free space, and Z_R denote the characteristic impedance of the substrate. The upper and lower surfaces of the substrate incorporate groove-type FSS with bandpass characteristics. These can be modeled using an equivalent inductance L_1, and two capacitances C_1 and C_2, connected in series with inductance L_1. Meanwhile, the middle layer of the substrate features a patch-type FSS with band-stop characteristics. This layer is modeled with an equivalent inductance L_2 and capacitance C_3, connected in series. According to the antenna radiation theory, when the total input impedance of the PRS matches the impedance of the free space wave, the electromagnetic waves from the radiation source can pass through the PRS without reflection, enabling maximum transmission. Conversely, any mismatch between the total input impedance of the PRS and the free space impedance will result in partial reflection. By appropriately designing and adjusting the PRS unit structure-particularly the impedance properties of the top and bottom surfaces, this impedance mismatch can be controlled to achieve the desired reflective or transmissive behavior.

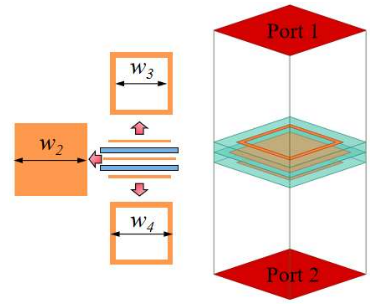

Fig. 8. The PRS unit structure.

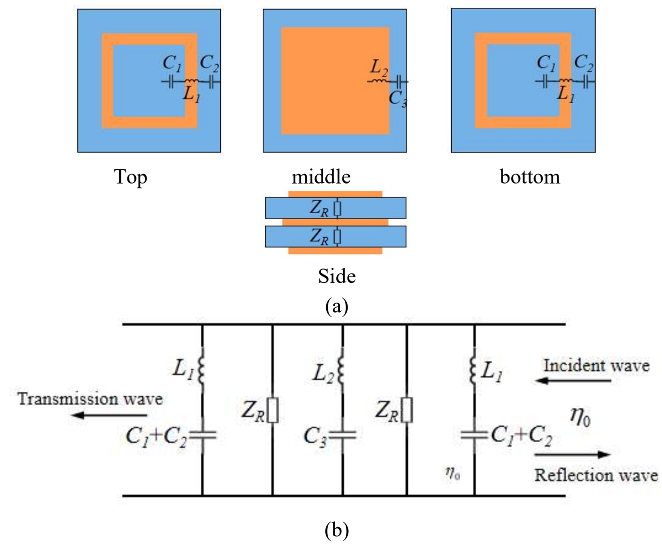

Fig. 9. The equivalent analysis of the unit model: (a) the equivalent model, (b) the equivalent circuit.

Fig. 10 presents the simulation results of the proposed PRS unit. A noticeable reflection band is observed in the range of around 6.0 GHz to 8.4 GHz. Reflection phase exhibits a positive slope at 7.6 GHz, indicating a forward reflection behavior. Similarly, the transmission phase shows a forward progression at 8.3 GHz, suggesting that reflection may cease near this frequency due to phase matching. Fig. 11 illustrates the reflection amplitude and phase response for varying values of w_2. As w_2 increases, the reflection effect decreases, and the reflection phase shifts forward in frequency. Among the optimal values, the configuration with w_2=8 mm provides the most favorable reflections characteristics.

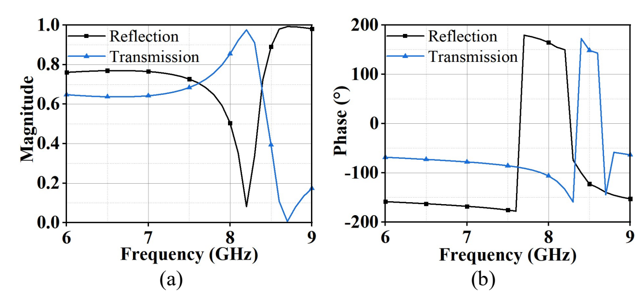

Fig. 10. Floquet port analysis of PRS unit: (a) reflection and transmission magnitude and (b) reflection and transmission phase.

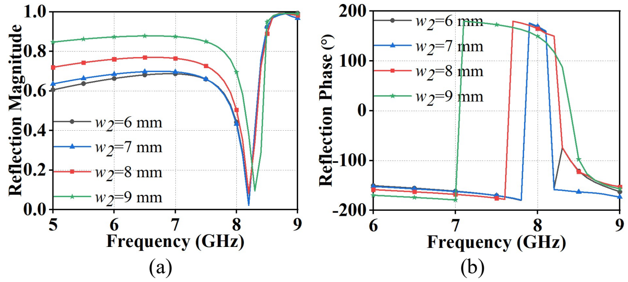

Fig. 11. Reflection at different w_2 sizes: (a) reflection amplitude, and (b) reflection phase.

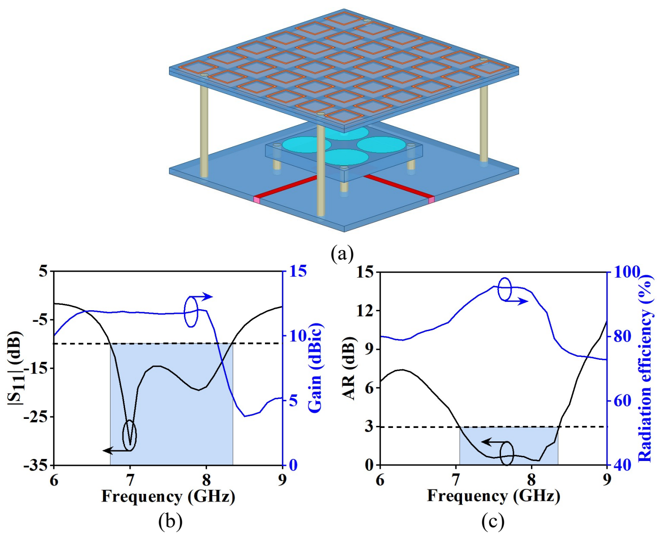

Fig.12. The design of the proposed broadband CP FPRCA: (a) the antenna model, (b) $|S_{11}|$ and gain, and (c) AR and radiation efficiency.

Combining the source antenna designed in the previous section with the PRS, a reasonable resonant cavity height is found, and its structure is shown in Fig. 12 (a). The simulation results are shown in Figs. 12 (b)-(c). Since there are two ports, $|S_{22}|$ and $|S_{11}|$ have the same parameters, only port 1 will be analyzed for data. The -10 dB IBW of the broadband CP FPRCA is 6.74 GHz ~8.33 GHz (21.1%), its 3-dB ARBW is 7.05 GHz ~8.33 GHz (16.7%), the peak gain (PG) is 12.1 dBic at 7.9 GHz, its 3-dB gain bandwidth is 6.74 GHz~8.16 GHz (19.1%), and its radiation efficiency is 79.4~95.6% in band. Its gain is increased by 2.0 dBic, 2.0 dBic, and 4.7 dBic respectively compared to the source antenna at 7.0 GHz, 7.5 GHz, and 8.0 GHz, and its ARBW is increased by 2.7% compared to the source antenna. The decrease in gain in the high frequency range is due to the phase hopping of PRS transmission. Overall, its gain and 3dB-ARBW are greatly improved compared to the source antenna.

D. Design and analysis of reconfigurable performance

Analysis of the source antenna shows that the feeder line is too long, preventing the excitation of CP. However, CP is successfully excited after adding a circular metasurface. The CMA analysis of metasurface revealed the potential for exciting CP waves due to their orthogonality. Modes 1 and 2 of the metasurface without added resistors resonate around 7 GHz, and the currents are orthogonal. If the polarization state is changed, the resonance state and current direction of Mode 1 and Mode 2 need to be altered. Therefore, the four metasurface are connected by introducing resistor to each other.

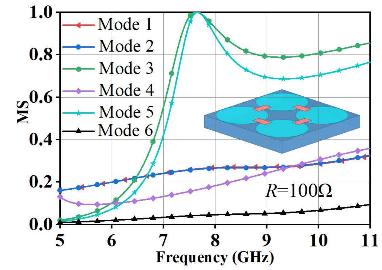

Fig. 13. The MSs with 2 × 2 circular metasurface with added resistors.

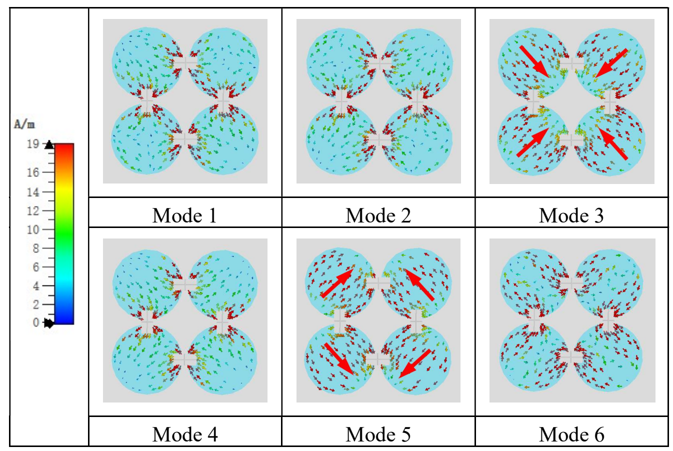

Fig. 14. Six modes current distributions of the 2×2 circular patch metasurface with added resistors at 7.5 GHz.

As shown in Fig. 13, taking 100 Ω as an example, the MS with introduced resistors only resonates in Modes 3 and 5, which are not orthogonal modes and only play an auxiliary role. The MS of Modes #1 and #2 is significantly lower than 0.707, and no resonance occurs in this frequency band. As shown in Fig. 14, the Modes #1 and #2 currents with added resistors are significantly disturbed and blocked. The currents of Modes #3 and #5 have an orthogonal distribution in the middle of the patch, but the auxiliary effect is weak, so the metasurface with added resistors has no potential to excite CP waves. The antenna performance was evaluated by introducing resistors with values of 51Ω, 100Ω, 151Ω, and 200Ω, as shown in Fig. 15 and Table II. Regarding the $|S_{11}|$, the resistance value had a significant impact. For gain, lower resistance resulted in reduced gain. In terms of the axial ratio, the resistance caused the axial ratio to approach 3 dB, diminishing the polarization reconfiguration effect. As for radiation efficiency, the overall efficiency is lower at both ends and higher in the middle with the efficiency still being lower than that of the configuration without the loaded resistors.

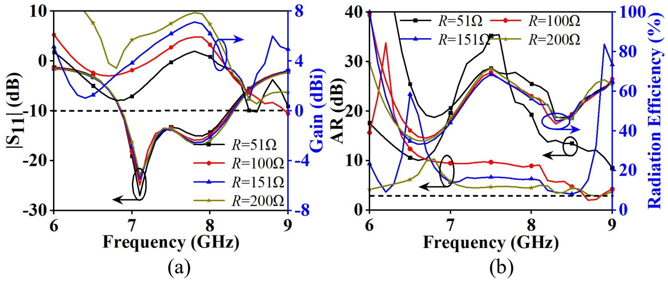

Fig. 15. Simulation data under different resistor values: (a) $|S_{11}|$ and gain, and (b) AR and radiation efficiency.

For the relationship between resistance and patch, assuming four patches are distributed in a 2×2 pattern, with adjacent patches connected in series with resistance R and structurally symmetrical (Z_1=Z_2=Z_3=Z_3=Z_{patch}), the equivalent impedance of the network as

$$Z_{eq} = Z_{patch} \parallel (R + Z_{patch} \parallel (R + Z_{patch} \parallel (R + Z_{patch} \parallel R))) \\ = \frac{Z_{patch}(2R + Z_{patch})}{2(Z_{patch} + R)} \tag{11}$$

During resonance, the surface mount reactance is 0, Z_{patch}=Z_{eq}, at this point, the equivalent impedance is purely resistive,

$$Z_{eq}\,|_{f=f_0} = \frac{R_{eq}(2R + R_{eq})}{2(R_{eq} + R)} \tag{12}$$

Adding a pure resistor does not change the impedance of the antenna itself, but rather the reactance component of the antenna itself remains unchanged, and the resonant frequency remains unchanged; The change is the equivalent input impedance of the antenna and load combination. Therefore, after adding a resistor, the resonant bandwidth of the antenna remains unchanged.

In fact, conductors and materials inevitably introduce a certain degree of loss. The definition of antenna loss power is

$$P_\sigma = \frac{I^2 R_\sigma}{2} \tag{13}$$

The antenna radiation efficiency is

$$\eta = \frac{P_r}{P_{in}} = \frac{P_r}{P_r + P_\sigma} = \frac{R_r}{R_r + R_\sigma} \tag{14}$$

where R_r is the radiation resistor, and R_σ is the loss resistor.

TABLE II
SIMULATION RESULTS UNDER RESISTORS STATES

Device	Value (Ω)	Pol.	IBW (%)	PG (dBi)	Max RE (%)
No resistor	/	CP	21.1	12.1	95.6
Resistors	51	LP	18.7	4.8	71.7
	100	LP	18.9	5.9	69.5
	151	LP	19.1	7.1	68.6
	200	LP	19.0	7.9	71.6

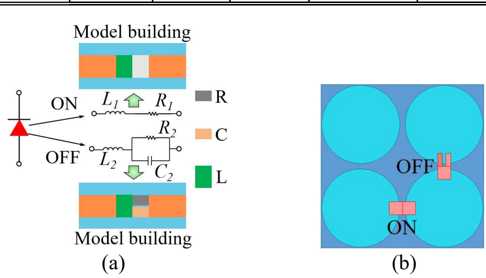

Fig. 16. The PIN diode connection method (a) and the embedding position of PIN diodes (b).

In addition to the loss of the antenna itself, induced currents in the floor introduce additional losses, which reduce the effective radiated power and, consequently, in the antenna gain. As shown in Equation (14), introducing a resistor (R) leads to a decrease in efficiency, higher resistance, the lower efficiency. Therefore, placing resistors on the floor results in a corresponding drop in both efficiency and gain. Sudden dips in the efficiency curve are caused by interference between the resistor placement and the feed point. Both theoretical analysis and simulation results confirm that efficiency decreases across all frequencies when resistors are introduced on the metasurface. This explains why such modifications lead to reduced efficiency.

In addition to the reconfigurability enabled by resistors, diodes are also used to achieve reconfigurable design. The proposed reconfigurable device is the SMP1340-079LF diode. Fig. 16(a) illustrates the ON/OFF connection method of the diode, while Fig. 16(b) indicates the placement of the reconfigurable device in the antenna. Among them, L_1=L_2=0.7 nH, R_1=0.8 Ω, R_2=5 kΩ, C_2=0.2 pF, using 3V voltage for control, its applicable frequency range is from 0.1 GHz to10 GHz.

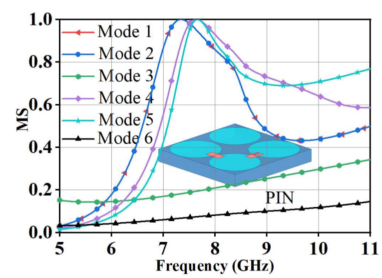

Fig. 17. The MSs with 2×2 circular metasurface with added PIN diodes.

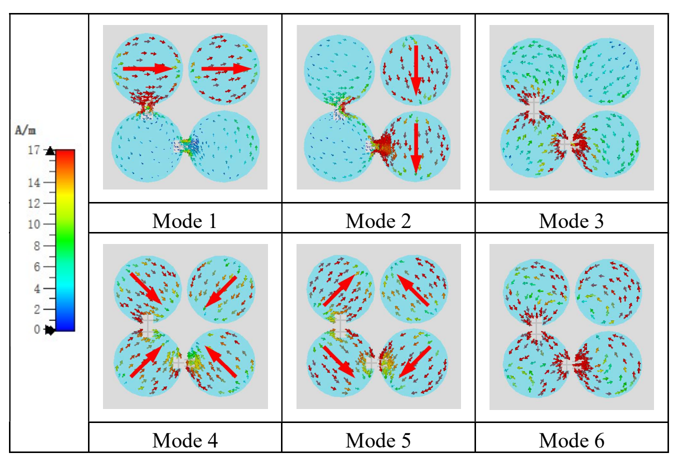

Fig. 18. Six modes current distributions of the 2×2 circular patch metasurface with added PIN diodes at 7.5 GHz.

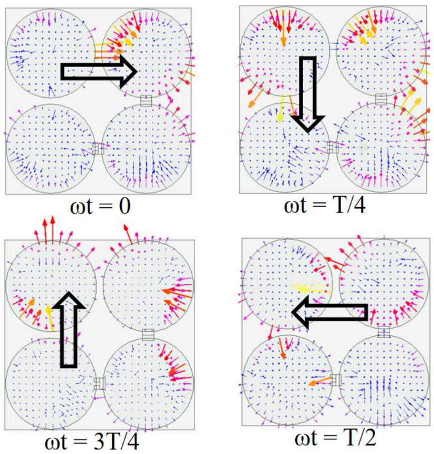

Fig. 19. Simulated surface vector electrical field distributions of the 2 × 2 circular patch metasurface with added PIN diodes at four different time phases for LHCP mode at 7.5 GHz (T is the time period).

The circular patch in the metasurface can be equivalent to a resonant unit. When the diode is connected between the patches, its equivalent impedance needs to be coupled with the inherent impedance of the patch. The final overall equivalent impedance as,

$$Z_{total} = Z_{patch} + Z_{diode-ON} + Z_{diode-OFF} \tag{15}$$

When the diode is turned OFF, it is approximately open circuit and has minimal impact on the inherent impedance of the chip. The overall equivalent impedance is still dominated by the capacitive/resonant characteristics of the chip. The cut-off state diode is distributed symmetrically in structure. When the diode is conducting, the patches are connected by a low impedance path, and the overall equivalent impedance is mainly inductive, which will change the current distribution of the patches, i.e. reverse the direction of the current, and achieve polarization switching.

The MS with integrated diodes is displayed in Fig. 17. The addition of resistors alters the current distribution on all circular patches, resulting in a transition from CP to LP. To achieve reconfigurability, diodes are strategically placed on the patches to selectively preserve certain current directions. In its original configuration, without reconfiguration, the device exhibits CP, with its radiation pattern showing RHCP at 180°, albeit with a relatively small RHCP component. Furthermore, considering the directional tendency of the FP antenna to radiate toward 0°, iterative simulations revealed that the reconfigured design can achieve LHCP performance. Based on Fig. 17, after adding diodes, Modes 1 and 2 still overlap and play as the main modes, while Modes 4 and 5 play an auxiliary role. Modes 3 and 6 remain inactive. As shown in Fig. 18, the mode currents of Modes 1 and 2 are orthogonal and reduced to half compared to the metasurface without diodes. Similarly, currents of Modes 4 and 5 are also orthogonally distributed. In contrast, the currents of Modes 3 and 6 are non-linear state and do not contribute to the operation. The electric field can be replaced by current, and since the *z*+ direction of the metasurface is the direction of wave propagation, its polarization state can be determined with the left hand in Fig. 18. Combined with the simulation results, the electric field distribution of the circular patch was examined, as shown in Fig. 19. Therefore, the mode analysis and its simulated electric field shows that the addition of diodes can achieve LHCP characteristics.

As illustrated in Fig. 20, after adding diodes, the antenna achieves -10 dB IBW of 6.74 GHz to 8.25 GHz (20.1%), 3-dB ARBW of 7.07 GHz to 8.35 GHz (16.6%). The PG reaches 11.9 dBic at 6.8 GHz, with a 3-dB gain bandwidth of 6.74 GHz to 8.05 GHz (17.7%). The radiation efficiency across the operating band ranges from 82.5% to 96.6%.

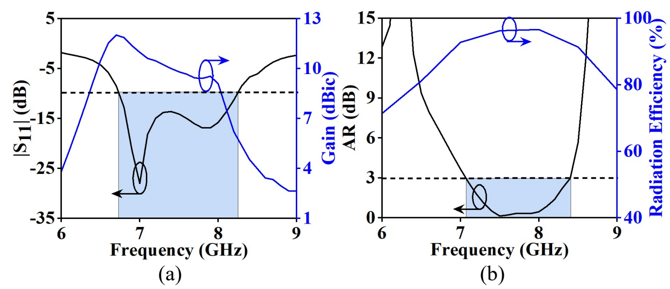

Fig. 20. The design of the proposed broadband FPRCA with added PIN diodes: (a) $|S_{11}|$ and gain, and (b) AR and radiation efficiency.

III. Antenna Measurement

To verify the feasibility of the designed antenna, as shown in Fig. 21(a), the broadband polarized reconfigurable FPRCA was fabricated and assembled with nylon screws. Fig. 22 shows the comparison between simulation and measurement for $|S_{11}|$, $|S_{22}|$, gain, and axial ratio without any loaded devices. Fig. 23 shows the comparison of $|S_{11}|$ and gain after connecting 100 Ω resistors. Fig. 24 illustrates the simulation and measurement comparison of $|S_{11}|$, gain, and axial ratio following the integration of diodes.

TABLE III
Comparison of The Antenna's Performances

Ref.	ARBW (%)	IBW (%)	PG (dBi)	Max. RE	Reconfigurable Components	Antenna Type	Reconfigurable Type
2024/[26]	1.5 1.6	5.1 6.2	4.40 4.80	90.0	2 capacitances	Patch antenna	Frequency
2025/[28]	N. A	5.7	6.80	N. A	8 PINs	Monopole antenna with FSS	Pattern
2024/[29]	N. A	4.8	5.96	70.0	12 PINs	Cavity-backed antenna	Pattern
2025/[30]	N. A	1.8	4.20	86.0	8 PINs	Loop antenna	Pattern
2024/[32]	11.2	11.7 (CP) 11.6 (LP)	4.20 5.35	N. A	6 PINs and 3 inductances	Dipole antenna with SIW	Polarization
2021/[33]	N. A	18.1 (HP) 16.8 (VP)	2.04 1.10	70.8	Dielectric resonator	Patch antenna	Polarization
2021/[34]	6.7	6.7(CP) 8.0(LP)	14.1 14.3	89	Mechanical rotation	FP antenna with metamaterial	Polarization

2025/[35]	N. A	11.5 3.8	5.87 7.74	88.0 95.9	2 PINs	Monopole antenna	Frequency and pattern
2021/[36]	30.0	21.0 (HP) 22.0 (VP)	3.66 4.38	N. A	16 PINs	Microstrip antenna with metasurface	Polarization and pattern
This work	17.2 / 18.3	20.6 (CP) 14.6 (LP-R) 21.0 (LHCP-PIN)	12.0 6.0 11.8	95.6 69.5 96.2	2 PINs and 4 resistors	FP antenna with metasurface	Polarization

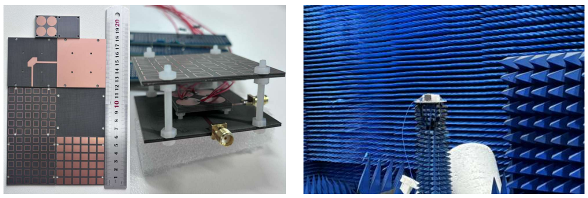

Fig. 21. Prototype and measurement of the proposed antenna: (a) Fabricated prototype, and (b) the microwave darkroom for measurement.

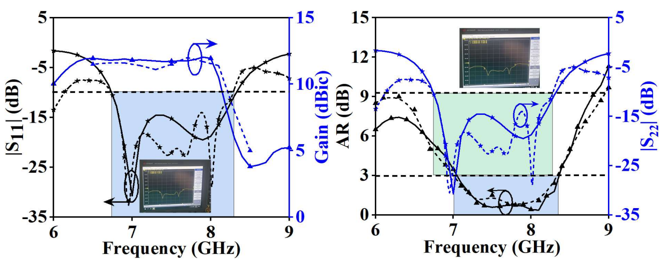

Fig. 22. Comparison of the simulated and measured results without loaded device: (a) $|S_{11}|$ and gain, and (b) $|S_{22}|$ and AR.

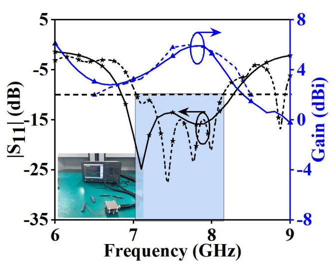

Fig. 23. The simulated and measured results of $|S_{11}|$ and gain with loaded resistors.

The measurement results show that the proposed antenna without any loaded devices achieves a -10 dB IBW of 20.6% (6.73 GHz-8.28 GHz), a 3-dB ARBW of 17.2% (6.9 GHz-8.2 GHz), a PG of 12.0 dBic at 7.7 GHz, and a 3-dB gain bandwidth of 19.7% (6.73 GHz-8.20 GHz). When 100 Ω resistors are connected, the -10 dB IBW is reduced to 14.6% (7.03 GHz-8.14 GHz), with a PG is 6.0 dBi at 7.7 GHz. With diodes loading, the antenna achieves a -10 dB IBW of 21.0% (6.79 GHz-8.38 GHz), a 3-dB ARBW of 18.4% (6.9 GHz-8.3 GHz), and the PG of 11.8 dBic at 6.9 GHz.

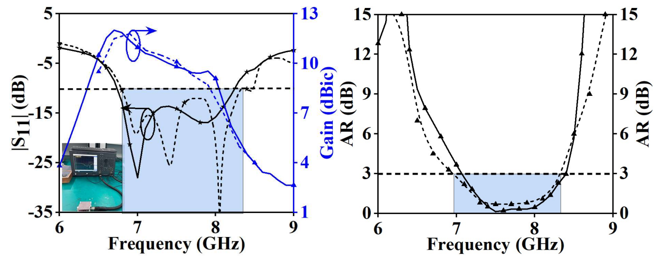

Fig. 24. Comparison of the simulated and measured results with loaded PIN diodes: (a) $|S_{11}|$ and gain, and (b) AR.

Figs. 25(a)-(b) present the simulated and measured LHCP and RHCP radiation patterns of the proposed antenna without any connected devices at 7.5 GHz. Figs. 25(c)-(d) show the simulated and measured E- and H-plane radiation patterns after loading 100 Ω resistor at 7.5 GHz. Figs. 25(e)-(f) display the simulated and measured LHCP and RHCP radiation patterns of the proposed antenna after diodes loading the same frequency.

For the unloaded device, the CP characteristics show that RHCP dominates in the 180°, 225°, and 320° directions. However, this behavior changes after the diodes are added, resulting in a shift in polarization from a mix of LHCP and LHCP to predominant LHCP. Apart from minor discrepancies due to soldering and installation errors, the introduction of small connecting wires slightly affects the impedance resonance point but does not significantly impact overall performance. The measured results closely align with the simulation results. A comparison with several polarization-reconfigurable antennas, as shown in Table III, indicates that the proposed antenna demonstrates relatively superior performance.

This work focuses on the design of a broadband polarization-reconfigurable Fabry-Perot resonant cavity antenna, with in-depth optimization of a 2 × 2 circular patch metasurface through CMA. The core characteristic mode performance is outstanding: at the center frequency of 7.5 GHz, the DM MS reaches 0.93 in the unloaded state, with the orthogonality of the dual dominant modes (current overlap integral) as low as 0.02, and an effective resonance bandwidth covering 6.32 GHz ~8.46 GHz (2.14 GHz), providing an excellent modal foundation for the stable excitation of CP. When PIN diodes are loaded, the DM MS remains 0.91 with a high retention rate of 97.8%, and the orthogonality is maintained at 0.03, enabling directional excitation of LHCP with a MRA of 90%. Notably, the effective resonance bandwidth still retains 1.94 GHz (6.41 GHz ~8.35 GHz) with minimal performance degradation. When 100 Ω resistors are integrated, the resonance of the dual dominant modes is precisely suppressed (MS drops to 0.32), successfully achieving LP switching with a RA of 88%. The entire design involves 6 modes (Modes 1~6), where the dominant and auxiliary modes have clear divisions of labor. Through a dual regulation path of "resistors suppressing orthogonal modes→ LP" and "diodes adjusting current direction→LHCP", flexible switching among three polarization states (CP/LP/LHCP) is realized. This design not only possesses excellent broadband modal regulation capability but also maintains high modal stability and regulation precision, fully meeting the application requirements of broadband, high-gain, and polarization-reconfigurable antennas.

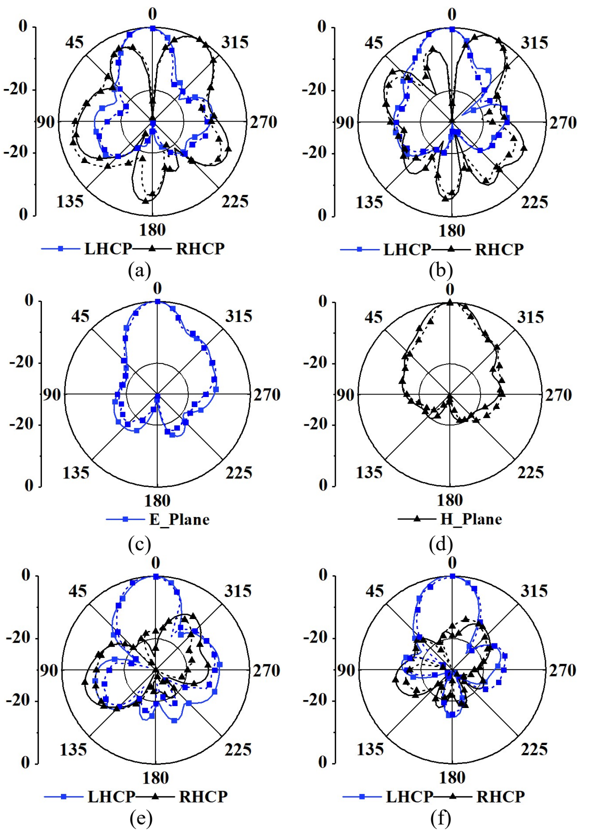

Fig. 25. The simulated and measured radiation patterns of the proposed antenna at 7.5 GHz: (a) xoz plane without loaded device, (b) yoz plane without loaded device, (c) E plane with loaded resistors, (d) H plane with loaded resistors, (e) xoz plane with loaded PIN diodes, and (f) yoz with loaded PIN diodes.

IV. Conclusion

A wideband, metasurface FPRCA with polarization reconfigured by diodes and resistors has been investigated in this paper. CMA optimizes the metasurface ' s orthogonal characteristic currents for stable CP excitation. Resistors enable straightforward CP-to-LP conversion, while diodes achieve left-handed CP (LHCP), with resistors offering simpler implementation and measurement. Unloaded, it delivers a 20.6% -10 dB IBW, 17.2% 3-dB ARBW, and 12.0 dBic peak gain. With 100 Ω resistors, it achieves 14.6% IBW and 6.0 dBi LP gain. Diode-loaded operation yields 21.0% IBW, 18.4% ARBW, and 11.8 dBic LHCP gain. CMA was conducted on the 2×2 metasurface both with and without these components, revealing that resistors and diodes alter the characteristic currents resistors suppress the orthogonal dominant modes while diodes reverse their current direction−thereby enabling flexible polarization control. Overall, the antenna adopts a practical, step-by-step design with a well-thought-out layout, synergistically integrating broadband operation, high gain, multi-state polarization reconfigurability (CP/LP/LHCP) and stable in-band performance. Superior to state-of-the-art designs − simpler than liquid metal-based ones, more comprehensive than dual-state solutions − it is a promising candidate for next-generation broadband communication systems.

References

[1] M. H. Hoang, T. Q. Van Hoang, H. P. Phan and T. P. Vuong, "Cavity-backed circular-polarized compact slot antenna for handheld UHF RFID reader," *IEEE Antennas Wireless Propag. Lett*., vol. 14, pp. 1439-1442, 2015.

[2] A. I. Abunjaileh, I. C. Hunter and A. H. Kemp, "A circuit-theoretic approach to the design of quadruple-mode broadband microstrip patch antennas," *IEEE Trans. Microw. Theory Techn.*, vol. 56, no. 4, pp. 896-900, Apr. 2008.

[3] J. Dacuna and R. Pous, "Low-profile patch antenna for RF identification applications," *IEEE Trans. Microw. Theory Techn.*, vol. 57, no. 5, pp. 1406-1410, May 2009.

[4] C. Sun, Z. Wu and B. Bai, "A novel compact wideband patch antenna for GNSS application," *IEEE Trans. Antennas Propag*., vol. 65, no. 12, pp. 7334-7339, Dec. 2017.

[5] F. Sultan and S. S. I. Mitu, "Superstrate-based beam scanning of a Fabry – Perot cavity antenna," *IEEE Antennas Wireless Propag. Lett*., vol. 15, pp. 1187-1190, 2016.

[6] L. Xu, Y. Liu and W. Zhang, "Wideband RCS reduction of dual-band Fabry-Perot cavity antenna using pancharatnam-berry phase coding metasurface and AMC surface," *IEEE Trans. Antennas Propag*., vol. 73, no. 6, pp. 4158-4163, Jun. 2025.

[7] Z. -G. Liu, R. -J. Yin, Z. -N. Ying, W. -B. Lu and K. -C. Tseng, "Dual-band and shared-aperture Fabry – Perot cavity antenna," *IEEE Antennas Wireless Propag. Lett*., vol. 20, no. 9, pp. 1686-1690, Sep. 2021.

[8] X. Gu et al., "Development, implementation, and characterization of a 64-element dual-polarized phased-array antenna module for 28-GHz high-speed data communications," *IEEE Trans. Microw. Theory Techn.*, vol. 67, no. 7, pp. 2975-2984, Jul. 2019.

[9] H. Sasaki, Y. Yagi, H. Fukumoto and D. Lee, "OAM-MIMO multiplexing transmission system for high-capacity wireless communications on millimeter-wave band," *IEEE Trans. Wireless Commun.*, vol. 23, no. 5, pp. 3990-4003, May 2024.

[10] X. Guo, Y. Luo, Z. N. Chen, N. Yan, W. An and K. Ma, "Multiple tri-beam low scanning loss metasurface antenna for wide-angle coverage by superposing focusing and periodic phases," *IEEE Trans. Microw. Theory Techn.*, vol. 71, no. 8, pp. 3466-3478, Aug. 2023

[11] Z. Zhou, Y. Li, Y. He, Z. Zhang and P. -Y. Chen, "A slender Fabry – Perot antenna for high-gain horizontally polarized omnidirectional radiation," *IEEE Trans. Antennas Propag*., vol. 69, no. 1, pp. 526-531, Jan. 2021.

[12] Z. Liu, J. Bornemann, D. F. Mamedes, S. Liu, X. Kong and X. Zhao, "A wideband Fabry-Pérot antenna with enhanced gain in the high-frequency operating band by adopting a truncated field correcting structure," *IEEE Trans. Antennas Propag*., vol. 69, no. 12, pp. 8221-8228, Dec. 2021.

[13] Q. Wang, A. Sihvola and J. Qi, "Ultrathin multimode Fabry – Perot cavity with wide phase resonance bandwidth enabled by janus partially reflective surface," *IEEE Antennas Wireless Propag. Lett*., vol. 22, no. 10, pp. 2412-2416, Oct. 2023.

[14] Y. Kong, Y. Ruan, H. Ebendorff-Heidepriem, Z. Xu and X. Shu, "Microstructured optical fibers-based Hybrid Fabry – Perot interferometer structure for improved strain sensing by vernier effect," *IEEE Trans. Instrum. Meas.*, vol. 71, pp. 1-14, 2022.

[15] N. Melouki, A. Hocini and T. A. Denidni, "High gain and wideband Fabry-Perot resonator antenna based on a compact single PRS layer," *IEEE Access*, vol. 10, pp. 96526-96537, 2022.

[16] Q. Wang, Y. Mu and J. Qi, "A novel reflection-mode Fabry–Perot cavity antenna with broadband high gain and large beam-scanning Angle by Janus Partially Reflective Surface," *IEEE Trans. Antennas Propag.*, vol. 71, no. 2, pp. 1350-1358, Feb. 2023.
[17] J. Qi, Q. Wang, F. Deng, Z. Zeng and J. Qiu, "Low-profile uni-cavity high-gain FPC antenna covering entire global 2.4 GHz and 5 GHz WiFi-bands using uncorrelated dual-band PRS and phase compensation AMC," *IEEE Trans. Antennas Propag.*, vol. 70, no. 11, pp. 10187-10198, Nov. 2022.
[18] Z. -G. Liu, C. Zhang, R. -J. Yin and W. -B. Lu, "Multifunctional low-profile Fabry–Perot resonator antenna integrated with solar cells," *IEEE Trans. Antennas Propag.*, vol. 70, no. 8, pp. 7175-7180, Aug. 2022.
[19] S. X. Ta and N. Nguyen-Trong, "Broadband dual-polarized Fabry–Perot antenna with simple feed for full-duplex applications," *IEEE Antennas Wireless Propag. Lett.*, vol. 21, no. 10, pp. 2095-2099, Oct. 2022.
[20] Z. Miao, N. Yan, F. Yang, Y. Luo and K. Ma, "A tri-band circularly polarized shared-aperture patch/Fabry–Pérot antenna for satellite communication," *IEEE Antennas Wireless Propag. Lett.*, vol. 23, no. 12, pp. 4423-4427, Dec. 2024.
[21] P. Xie, G. Wang, H. Li, J. Liang and X. Gao, "Circularly polarized Fabry-Perot antenna employing a receiver–transmitter polarization conversion metasurface," *IEEE Trans. Antennas Propag.*, vol. 68, no. 4, pp. 3213-3218, Apr. 2020.
[22] P. Xie, G. Wang, X. Zou and B. Zong, "Gain and AR Improvements of the Wideband Circularly Polarized Fabry-Perot Resonator Antenna," *IEEE Trans. Antennas Propag.*, vol. 69, no. 10, pp. 6965-6970, Oct. 2021.
[23] M. Ashfaq, M. U. Khan, T. Farooqi and R. K. Arya, "Liquid-based reconfigurable Fabry–Pérot cavity antenna for beam-steering applications," *IEEE Antennas Wireless Propag. Lett.* vol. 23, no. 11, pp. 3744-3748, Nov. 2024.
[24] J. Su, C. Lv, M. Qu and H. Yu, "A low-profile reconfigurable radiation-type metasurface for wide-angle beam scanning based on true-time-delay line feed network," *IEEE Antennas Wireless Propag. Lett.*, vol. 23, no. 2, pp. 773-777, Feb. 2024.
[25] Y. -G. Jeon, G. -R. Yun, J. Kim and D. Kim, "Polarization reconfigurable high-gain Fabry–Perot cavity antenna," *IEEE Trans. Antennas Propag.*, vol. 70, no. 9, pp. 7727-7734, Sep. 2022.
[26] S. Han, Z. Wang and Y. Dong, "Miniaturized circularly polarized reconfigurable capacitance-loaded patch antenna," *IEEE Antennas Wireless Propag. Lett.*, vol. 23, no. 4, pp. 1226-1230, Apr. 2024.
[27] T. K. Nguyen, C. D. Bui, A. Narbudowicz and N. Nguyen-Trong, "Frequency-reconfigurable antenna with wide- and narrowband modes for Sub-6 GHz cognitive radio," *IEEE Antennas Wireless Propag. Lett.*, vol. 22, no. 1, pp. 64-68, Jan. 2023.
[28] P. Danuor, J. -I. Moon, J. -N. Lee and Y. -B. Jung, "A pattern-reconfigurable antenna using tunable band-stop FSS with reduced switching elements," *IEEE Antennas Wireless Propag. Lett.*, vol. 24, no. 1, pp. 172-176, Jan. 2025.
[29] T. -G. Huang, F. -C. Chen, K. -R. Xiang, L. -Y. Wei and W. -F. Zeng, "Pattern-reconfigurable cavity-backed antenna based on radiant metal blocks," *IEEE Antennas Wireless Propag. Lett.*, vol. 23, no. 12, pp. 4553-4557, Dec. 2024.
[30] Y. Huang, Z. Liu, X. Kong, H. Zhou, Z. Lei and Y. Wang, "A Dual-Polarized 3-D Radiation Pattern-Reconfigurable Fabry–Perot Antenna Based on Liquid-Based Partially Reflective Surface," *IEEE Antennas Wireless Propag. Lett.*, vol. 24, no. 12, pp. 4895-4899, Dec. 2025.
[31] A. Jafargholi, M. Safaei and R. Fleury, "A Reconfigurable Pattern Loop Antenna for Wireless Applications," *IEEE Antennas Wireless Propag. Lett.*, vol. 24, no. 7, pp. 1670-1674, Jul. 2025.
[32] R. K. Jaiswal, Aakash, A. K. Ojha, C. -Y. -D. Sim and K. V. Srivastava, "Wideband low-profile endfire antenna with polarization reconfigurability," *IEEE Trans. Circuits Syst. II-Express Briefs*, vol. 71, no. 4, pp. 1984-1988, Apr. 2024.
[33] X. Liu, K. W. Leung and N. Yang, "Wideband horizontally polarized omnidirectional cylindrical dielectric resonator antenna for polarization reconfigurable design," *IEEE Trans. Antennas Propag.*, vol. 69, no. 11, pp. 7333-7342, Nov. 2021.
[34] F. Wu and K. M. Luk, "Circular polarization and reconfigurability of Fabry–Pérot resonator antenna through metamaterial-loaded cavity," *IEEE Trans. Antennas Propag.*, vol. 67, no. 4, pp. 2196-2208, Apr. 2019.
[35] Y. Yuan, S. Jammy Chen and C. Fumeaux, "Frequency- and pattern-reconfigurable antenna pair fed by a frequency-swappable diplexer," *IEEE Trans. Antennas Propag.*, vol. 73, no. 5, pp. 2780-2790, May 2025.
[36] W. Li, Y. M. Wang, Y. Hei, B. Li and X. Shi, "A compact low-profile reconfigurable metasurface antenna with polarization and pattern diversities," *IEEE Antennas Wireless Propag. Lett.*, vol. 20, no. 7, pp. 1170-1174, Jul. 2021.
[37] Y. Liu, Z. Wang and Y. Dong, "Vertically polarized, pattern-reconfigurable, Yagi–Uda dielectric resonator antenna," *IEEE Antennas Wireless Propag. Lett.*, vol. 24, no. 4, pp. 1018-1022, Apr. 2025.
[38] Z. Ding, J. Li, J. Cao, H. Wang, M. Y. -W. Chia and N. Nasimuddin, "Wideband dual-polarized metasurface antenna with polarization reconfigurable controlled by diode and resistor, featuring low RCS," *IEEE Antennas Wireless Propag. Lett.*, vol. 24, no. 5, pp. 1208-1212, May 2025.
[39] H. Xing et al., "Three-polarization-reconfigurable antenna array implemented by liquid metal," *IEEE Antennas Wireless Propag. Lett.*, vol. 23, no. 1, pp. 374-378, Jan. 2024.
[40] C. Guo, Z. Zhang, X. Fu and J. Wang, "A frequency-reconfigurable antenna with filtering characteristics using characteristic mode Analysis," *IEEE Antennas Wireless Propag. Lett.*, vol. 22, no. 8, pp. 1793-1797, Aug. 2023.
[41] K. Gao, Y. Zhou, T. Li, H. Yang, S. Li and X. Cao, "Design of Frequency-Reconfigurable and Decoupled Dual-Port Single-Radiating Patch Antennas Using Characteristic Mode Analysis," *IEEE Trans. Antennas Propag.*, vol. 72, no. 9, pp. 7068-7076, Sep. 2024.
[42] Z. Chen, W. Hu, K. Wei, L. Wen, Z. Hu and S. Gao, "A wideband polarization-reconfigurable antenna using the combined characteristic modes and common/differential modes," *IEEE Antennas Wireless Propag. Lett.*, vol. 23, no. 3, pp. 1139-1143, Mar. 2024.
[43] Z. Ding, Z. Dai, J. Cao, H. Wang, Nasimuddin and M. Y. -W. Chia, "A polarization reconfiguration wideband Fabry-Perot resonator antenna with resistor manipulation," *2025 IEEE MTT-S International Microwave Workshop Series On Advanced Materials and Processes for RF and THz Applications (IMWS-AMP)*, Wuxi, China, 2025.
[44] G. V. Trentini, "Partially reflecting sheet arrays," IRE *Trans. Antennas Propag.*, vol. 4, no. 4, pp. 666-671, Oct. 1956.
[45] T. Li and Z. N. Chen, "Shared-surface dual-band antenna for 5G applications," *IEEE Trans. Antennas Propag.*, vol. 68, no. 2, pp. 1128-1133, Feb. 2020.
[46] X. Wang, L. Guo, W. Zhou and Q. Zhang, "A double-layer multimode metasurface antenna using characteristic mode analysis," *IEEE Antennas Wireless Propag. Lett.*, vol. 23, no. 10, pp. 3237-3241, Oct. 2024.

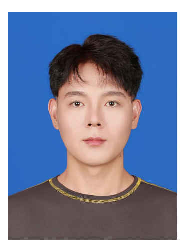

Zhendong Ding received the B.Sc. degree in electronic information engineering from Nanjing Normal University Zhongbei College of China in 2015, received the M.Eng. degree in instrumentation engineering from Nanjing Forestry University, Nanjing, China, in 2019, and received the Ph.D. degree in Electronic Science and Technology from Nanjing University of Science and Technology, Nanjing, China, in 2025.

From June 2015 to August 2017, he worked as an assistant engineer at Nanjing Keruida Electronic Equipment Co., Ltd. From July 2019 to August 2020, he worked as an engineering technician at Nanjing Metro Operation Co., Ltd. From November 2013 to October 2024, he was sponsored by CSC as a doctoral student for joint training and learning at Institute for Infocomm Research, A*STAR in Singapore. Currently, he is working as a postdoctor at South China University of Technology. His main research interests are the design and optimization of microstrip antennas, metasurface antennas, reconfigurable antennas, and photonic crystals.

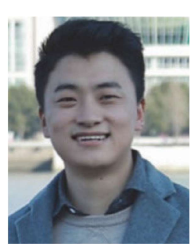

Jiawang Li (Graduate Student Member, IEEE) received the B.S. degree in information and communication engineering from Harbin Engineering University, Harbin, China, in 2019, and the M.S. degree in the electromagnetic field and microwave technology from the State Key Laboratory of Millimeter Waves, Southeast University, Nanjing, China, in 2022. He is currently pursuing the Ph.D. degree with the Communication Group, Department of Electrical and Information Technology, Lund University, Lund, Sweden.

In 2020, he interned with Telefonaktiebolaget LM Ericsson, Beijing, China. From 2022 to 2023, he was with the CBG Department, Huawei Technolo- gies Company Ltd., Shanghai, China, as a Senior Engineer. His current research interests include antennas, millimeter-wave radar, radio frequency (RF) systems, wireless power transfer systems, beamforming algorithms, and channels. Mr. Li was a recipient of the Outstanding Master's Thesis Award from the Chinese Institute of Electronics in 2023 and the Rohde and Schwarz Graduate Fellowship in 2021.

Hao Wang (Member, IEEE) received the B.S. and Ph.D. degrees in electrical engineering from Nanjing University of Science and Technology, Nanjing, China, in 2002 and 2009, respectively.

Currently, he is a Professor at the School of Electronic and Optical Engineering, Nanjing University of Science and Technology. His research interests include microstrip antennas for wireless communications, terminal antenna subsystems for compass navigation satellite systems, millimeter-wave antenna subsystems, LTCC-based system-on-package technology, and antennas in package.

Nasimuddin Nasimuddin (Senior Member, IEEE) received his M.Tech. and Ph.D. degrees from the University of Delhi in 1998 and 2004, respectively. He was a Senior Research Fellow at the University of Delhi from 1999 to 2003 and subsequently held the position of Australian Postdoctoral Research Fellow at Macquarie University, Sydney, from 2004 to 2006. He is currently a Principal Scientist at the Institute for Infocomm Research (I²R), A*STAR, Singapore. Dr. Nasimuddin is a prolific contributor to the field, with over 260 research publications, four granted patents, and four additional patents filed. He has edited three books, including two chapters. His outstanding work has earned him recognition as one of the Stanford's Top 2% of scientists in 2023 2024, and 2025.
He is a Senior Member of the IEEE and its Antennas and Propagation Society (AP-S), Microwave Theory and Technology Society (MTT-S), and Geoscience and Remote Sensing Society (GRSS), as well as a Life Fellow of the WAMS Society. His accolades include the URSI Young Scientist Award (2005) and multiple IEEE AP-T/APPL Exceptional Performance Reviewer Awards. He serves as an Associate Editor for the IEEE Open Journal of Antennas and Propagation (OJAP), Editor-in-Chief of Wireless and Communication Letters and is a member of the editorial boards of several leading journals in antennas and propagation. He also served as Chair of the IEEE Singapore MTT/AP Joint Chapter from 2021 to 2022.

Wenjie Feng (Senior Member, IEEE) was born in Shangqiu, Henan, China, in 1985. He received the B.Sc. degree from the First Aeronautic College of the Airforce, Xinyang, China, in 2008, and the M.Sc. and Ph.D. degrees from Nanjing University of Science and Technology (NUST), Nanjing, China, in 2010 and 2013, respectively.

From July 2017 to September 2017, he was a Research Fellow with the City University of Hong Kong, Hong Kong. From October 2010 to March 2011, he was an exchange student with the Institute of High Frequency Engineering, Technische Universität München, Munich, Germany. He is currently a Professor with NUST, and also a Professor with South China University of Technology, Guangzhou, China. He has authored or co-authored over 100 IEEE journal articles (including 70 IEEE TRANSACTIONS papers) and 80 conference papers. His research interests include wideband circuits and technologies, microwave and millimeter-wave circuits and components, circuits interconnection, and packaging.

Dr. Feng was a recipient of the National Science Fund for Excellent Young Scholars in 2018, the Young Scientist Award of ACES-China 2018, and a reviewer for over 20 internationally refereed journals and conferences. He currently serves as an Associate Editor for IET Microwaves, Antennas & Propagation, IET Electronics Letters, and International Journal of Electronics.

Wenquan Che (Fellow, IEEE) received the B.Sc. degree from the East China Institute of Science and Technology, Nanjing, China, in 1990, the M.Sc. degree from the Nanjing University of Science and Technology (NUST), Nanjing, in 1995, and the Ph.D. degree from the City University of Hong Kong (CityU), Hong Kong, in 2003.

From 1995 to 2018, she was a Lecturer, an Associate Professor, and a Professor with NUST. From March 2002 to September 2002, she was a Visiting Scholar with the Polytechnique de Montréal, Montréal, QC, Canada. From 2005 to 2006 and 2009 to 2016, she was a Research Fellow and a Visiting Professor with CityU. From 2007 to 2008, she conducted academic research with the Institute of High Frequency Technology, Technische Universität München, Munich, Germany. From summer 2005 to summer 2006 and from summer 2009 to summer 2012, she was with CityU as a Research Fellow and a Visiting Professor. From 2013 to 2018, she was the Executive Dean of the Elite Education College, NUST. In 2018, she joined the South China University of Technology, Guangzhou, China, as a Full Professor. She has authored or co-authored over 300 internationally refereed journal articles and over 150 international conference papers. Her current research interests include microwave and millimeter-wave circuits and systems, microwave monolithic integrated circuits, antenna technologies, and the medical applications of microwave technologies.

Dr. Che was a recipient of the 2007 Humboldt Research Fellowship by the Alexander von Humboldt Foundation of Germany, the fifth China Young Female Scientists Award in 2008, and the Distinguished Young Scientist Award by the National Natural Science Foundation Committee of China in 2012. She is the Administrative Committee Member from 2018 to 2026. She is a Reviewer of the IEEE TRANSACTIONS ON MICROWAVE THEORY AND TECHNIQUES, IEEE TRANSACTIONS ON ANTENNAS AND PROPAGATION, IEEE TRANSACTIONS ON INDUSTRIAL ELECTRONICS, and IEEE MICROWAVE AND WIRELESS COMPONENTS LETTERS. She has been the Editor-in-Chief of Microwave and Optical Technology Letters since 2019.

Quan Xue (Fellow, IEEE) received the B.Sc., M.Sc., and Ph.D. degrees in electronic engineering from the University of Electronic Science and Technology of China (UESTC), Chengdu, China, in 1988, 1991, and 1993, respectively. In 1993, he joined the UESTC, as a Lecturer. He became a Professor in 1997. From October 1997 to October 1998, he was a Research Associate and then a Research Fellow with The Chinese University of Hong Kong, Hong Kong. In 1999, he joined the City University of Hong Kong, Hong Kong, and was the Chair Professor of Microwave Engineering. He also served with the University as the Associate Vice President (Innovation Advancement and China Office) from June 2011 to January 2015, the Director of the Information and Communication Technology Center and the Deputy Director of the State Key Laboratory of Millimeter Waves, Hong Kong. In 2017, he joined South China University of Technology, Guangzhou, China, where he is currently a Professor and also serves as the Dean of the School of Electronic and Information Engineering, the Dean of the School of Microelectronics, and the Director the Guangdong Provincial Key Laboratory of Millimeter Wave and Terahertz. He is also the Chief Scientist of 2012 Labs, Huawei Technologies, and a member with the National 6G Technology General Expert Group. He has authored or co-authored over 400 internationally refereed journal articles and over 150 international conference papers. He is the co-inventor of more than 20 granted Chinese patents and more than 30 granted U.S. patents, five of which have been transferred. His research interests include microwave/millimeter-wave/THz passive components, active components, antennas, and microwave monolithic integrated circuits, and radio frequency integrated circuits.

Dr. Xue was the winner of the 2017 H. A. Wheeler Applications Prize Paper Award. He served the IEEE as an AdCom Member for MTT-S from 2011 to 2013. He served as an Associate Editor for IEEE TRANSACTIONS ON MICROWAVE THEORY AND TECHNIQUES from 2010 to 2013, an Editor for International Journal of Antennas and Propagation from 2010 to 2013, and an Associate Editor for IEEE TRANSACTIONS ON INDUSTRIAL ELECTRONICS from 2010 to 2015 and IEEE TRANSACTIONS ON ANTENNA AND PROPAGATIONS in 2016. He was appointed as a Distinguished Microwave Lecturer for the IEEE Microwave Theory and Techniques Society from 2022 to 2024.